Lower-Defect Graphene Oxide Nanoribbons from Multiwalled Carbon Nanotubes

Amanda L. Higginbotham, Dmitry V. Kosynkin, Alexander Sinitskii, Zhengzong Sun, and James M. Tour*

Departments of Chemistry and Mechanical Engineering and Materials Science and the Smalley Institute for Nanoscale Science and Technology, Rice University, MS 222, 6100 Main Street, Houston, Texas 77005

ABSTRACT An improved method is described for the production of graphene oxide nanoribbons (GONRs) *via* longitudinal unzipping of multiwalled carbon nanotubes. The method produces GONRs with fewer defects and/or holes on the basal plane, maintains narrow ribbons <100 nm wide, and maximizes the high aspect ratio. Changes in the reaction conditions such as acid content, time, and temperature were investigated. The new, optimized method which introduces a second, weaker acid into the system, improves the selectivity of the oxidative unzipping presumably by *in situ* protection of the vicinal diols formed on the basal plane of graphene during the oxidation, and thereby prevents their overoxidation and subsequent hole generation. The optimized GONRs exhibit increased electrical conductivity over those chemically reduced nanoribbons produced by previously reported procedures.

Graphene, carbon sheets with a planar lattice, is a semimetal that has been proven to exhibit charge carrying properties that rival or surpass all known materials used in electronics applications.[1,2] Furthermore, the flexible yet strong material is an outstanding heat conductor and gas barrier which also makes it of interest for composite applications.[3,4] Graphene nanoribbons (GNRs) are strips of graphene with a high length-to-width ratio and straight edges. The electron confinement within the ribbons results in a width dependence of the electronic properties; they transform from semimetallic to semiconducting as the width decreases, especially below 10 nm.[5,6] Experimentally, microscopic quantities of few-layer graphene nanoribbons were made available through several processes including microfabrication on graphite surfaces followed by exfoliation,[6] exfoliation of bulk graphite in the presence of surfactants,[7] or plasma etching of multiwalled carbon nanotubes (MWCNTs) partially imbedded in a layer of protective polymer.[8] The first method for producing macroscopic quantities of graphene nanoribbons was reported through a chemical vapor deposition (CVD) growth process that resulted in ribbons containing multiple layers of graphene with kinked morphology and irregular atomic structure.[9] Recently, our research group reported a high-yielding procedure for production of large amounts of single and few-layer GNRs through oxidative longitudinal unzipping of MWCNTs in sulfuric acid.[10] It was found that potassium permanganate (KMnO₄) is an unusually selective oxidant for longitudinal cleavage of MWCNTs; however, other strong oxidants based on high oxidation states of transition metals that

give cis-oxidation of double bonds (*i.e.*, OsO₄ and FeO₄²⁻) are expected to effect the same longitudinal unzipping.[10] The GNRs obtained from MWCNTs possess straight edges and high aspect ratios with no significant shortening of the parent tubes. Since the unzipping process is oxidative, the composition is similar to graphene oxide (GO), therefore these nanoribbons are termed graphene oxide nanoribbons (GONRs). Both GO and GONRs possess oxygen-containing functionalities such as carbonyls, carboxyls, epoxides, and hydroxyls at the edges and surface[11] and are highly soluble in water and polar organic solvents. It was also found that the degree of permanganate-induced unzipping can be controlled by adjusting the amount of oxidant used in the reaction. As with GO, the GONRs can be chemically reduced with hydrazine (N₂H₄) resulting in significantly lower oxygen content and restoration of much of the $\pi-\pi$ conjugation, noted by recovery of electrical conductivity and a dramatic increase in absorption intensity across the entire UV−vis region.[10]

*Address correspondence to tour@rice.edu.

Among the GONRs produced using the previously described method,[10] ribbons <100 nm wide were rarely observed in the product. Since a high yield of MWCNT opening and subsequent exfoliation of the GONR layers is obtained, narrow GONRs <100 nm wide are most likely oxidatively consumed during the oxidation process. Excessive oxidation must occur that not only destroys the more reactive, narrow ribbons derived from the inner tubes but also disrupts contiguous regions of the basal plane of the wider ribbons, causing holes of various shapes and sizes. These holes, which also form during the oxidation of graphite, have been identified as lattice distortions in the atomic structure after oxidation of graphite.[12] Upon chemical reduction of the oxygen functionalities (*i.e.*, hydrazine treatment), the lattice distortions (such as holes) remain and cause substantially lower conductance and carrier mobilities in the reduction product of GO, termed chemically converted graphene (CCG), when compared to the conductance and mobility in exfoliation-derived graphene.[13] In addition, holes in the basal planes could be deleterious for applications relying on the tensile strength or gas impermeability of the material.

In this work, an improved method is described for the production of GONRs *via* longitudinal unzipping of MWCNTs that results in GONRs with fewer defects and/or holes on the basal plane, as well as maintaining narrow ribbons <100 nm wide and maximizing the high aspect ratio. Changes in the reaction conditions such as acid content, time, and temperature were investigated. The new, optimized method improves the selectivity of the oxidative unzipping presumably by *in situ* protection of the vicinal diols formed on the basal plane of graphene during the oxidation and thereby prevents their overoxidation to diones and the subsequent hole generation.

Variations of Reaction Conditions for Nanoribbon Formation. To further understand the reaction mechanism and to study the importance of each variable, a series of reactions were carried out with variations in the acid medium, temperature, and time of the reaction. The reaction conditions and results are summarized in Table 1. Listed in the table are the weight gain of the isolated product (wt %, relative to the weight of the starting MWCNTs), the representative transmission electron microscopy (TEM) and scanning electron microscopy (SEM) images of bulk, powder samples, the C:O atomic concentration ratio determined by XPS, the TGA wt % remaining at 250 and 950 °C under inert gas, λ_{max} as determined by the UV analysis of a dilute aqueous solution, and overall conclusions. The weight gain of the product, C:O XPS ratio, and TGA wt % together give an indication of the degree of oxidation; a highly oxidized sample will have an increase in weight of 50−140%, a low C:O ratio, and less weight remaining by TGA, all due to the presence of oxygen-containing functional groups on the edges and ba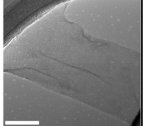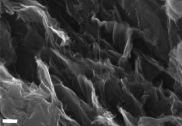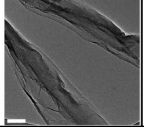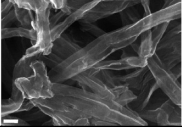sal plane. The UV λ_{max} indicates the level of π-conjugation remaining in the system, and hence the relative degree of oxidation; highly conjugated graphene-like material will have a higher λ_{max} (~275 nm) while material with a disrupted π-network and greater number of sp^3 carbons will have a blue-shifted λ_{max} (~235 nm). High resolution SEM and TEM images as well as the full UV−vis absorption spectra and XPS survey scans with atomic concentrations of all reaction products listed in Table 1 and starting material MWCNTs are given in the Supporting Information.
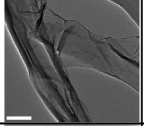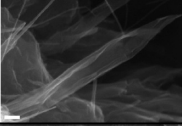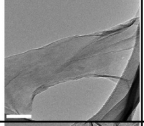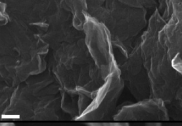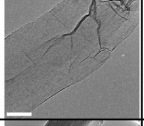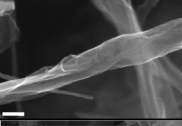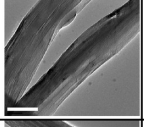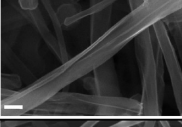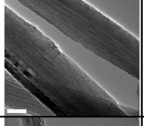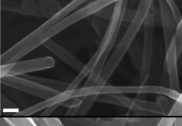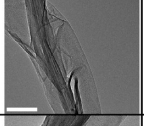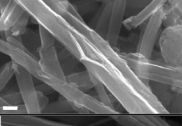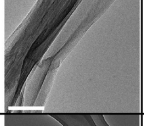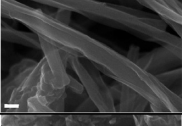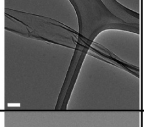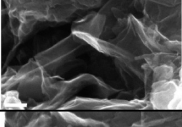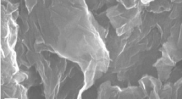
All reactions used $KMnO_4$ as the oxidizing agent. Reaction 1 was carried out using the method previously published[10] and is given as a reference for comparison. Reactions 2−5 were prepared under similar conditions with variations in the reaction time and temperature. Reactions 6−12 varied the acid medium, as well as the time or temperature.

Reactions 1−5 used concentrated H_2SO_4, 5 weight equivalents of $KMnO_4$ relative to the weight of MWCNTs (5× $KMnO_4$), and varied reaction temperatures from 22 to 100 °C. A moderate excess of $KMnO_4$ is used relative to the theoretical limit of 4.4× $KMnO_4$ for complete oxidation of all alkenes in the case of infinite size graphite crystals. The results indicate that elevated temperatures are necessary for formation of GONRs when the reaction is run for 1−2 h. Exfoliated and highly oxidized GONRs are formed in all reactions where the temperature is maintained above 60 °C; however, at ≥60 °C, the actual reaction temperature did not appear to have a significant effect on the resulting GONR properties. The products of reactions 1, 3, and 4 all had ~100 wt % increase upon isolation of the product, a C:O ratio of ~1.5:1, and a TGA weight loss of 50−60 wt % at 950 °C. Reaction 2, which was conducted at room temperature, resulted in stacked ribbons and partially opened tubes with lower levels of oxidation; the weight increase was only 26 wt %, and the C:O ratio nearly doubled at 2.6:1. In addition, the UV λ_{max} was red-shifted from the other four reactions (262 nm compared to ~235 nm for the more exfoliated ribbons). Therefore, the necessity for heat to complete the exfoliation and oxidation is highlighted in this set of experiments.

Reaction 6 used 10% fuming sulfuric acid (oleum at 10% SO_3 content in H_2SO_4). The reaction was run with 5× $KMnO_4$ at room temperature for 24 h, but failed to p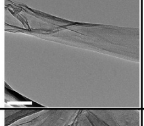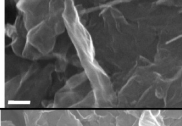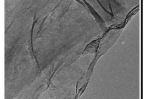roduce exfoliated ribbons. It is hypothesized that the oleum decomposes $KMnO_4$ before it reacts with the MWCNTs. Strong acid environments, especially in the presence of SO_3, will cause decomposition of permanganate to afford ozone and oxygen.[14] SEM imaging and TEM imaging reveal partially opened MWCNTs for the product of reaction 6 with minimal oxidation: no weight gain upon isolation, high C:O ratio of 16:1, TGA weight loss of 10 wt % at 950 °C, and a red-shifted UV λ_{max} of 278 nm were observed.

TABLE 1. Summary of Reaction Conditions and Results

Reaction	Prep. Conditions[b]	Wt%[c]	TEM[d]	SEM[d]	C:O Ratio (XPS)	TGA[e] Wt% @ 250 °C	TGA[f] Wt% @ 950 °C	UV λ_{max}[g] (nm)	Conclusions
1[a]	5× KMnO₄ in H₂SO₄ 22 °C → 70 °C 2 h	140			1.5:1	84	52	234	Exfoliated Ribbons Fully opened, high oxidation
2	5× KMnO₄ in H₂SO₄ 22 °C, 2 h	26			2.6:1	66	44	262	Stacked Ribbons Partially opened, light oxidation
3	5× KMnO₄ in H₂SO₄ 60 °C, 2 h	105			1.4:1	67	40	237	Exfoliated Ribbons Fully opened, high oxidation
4	5× KMnO₄ in H₂SO₄ 85 °C, 2 h	95			1.5:1	63	31	233	Exfoliated Ribbons Fully opened, high oxidation
5	5× KMnO₄ in H₂SO₄ 100 °C, 2 h	36			1.7:1	72	42	235	Exfoliated Ribbons Fully opened, high oxidation
6	5× KMnO₄ in 10% oleum 22 °C, 24 h	0			16.1:1	99	90	278	Stacked Ribbons & Tubes Partially opened, no oxidation
7	5× KMnO₄ in TFA/TFAA 22 °C, 24 h	0			7.6:1	100	94	270	Stacked Ribbons & Tubes Minor unzipping, low oxidation
8	5× KMnO₄ in 1:1 H₂SO₄:TFA 22 °C, 24 h	34			4.0:1	89	74	265	Stacked Ribbons & Tubes Partial unzipping, low oxidation
9	5× KMnO₄ in 9:1 H₂SO₄:TFA 22 °C, 24 h	60			1.5:1	71	49	236	Stacked Ribbons Opened, high oxidation, not exfoliated
10[h]	5× KMnO₄ in 9:1 H₂SO₄:TFA 65 °C, 2 h	65			1.8:1	66	43	245	Exfoliated Ribbons Fully opened, high oxidation with low defects
11[i]	5× KMnO₄ in 9:1 H₂SO₄:H₃PO₄ 65 °C, 2 h	78			1.6:1	63	42	235	Exfoliated Ribbons Fully opened, high oxidation with low defects
12	8× KMnO₄ in 9:1 H₂SO₄:H₃PO₄ 65 °C, 2 h	43			1.4:1	55	18	227	Exfoliated Ribbons & Sheets Fully opened, high oxidation

[a]Previously published conditions and results.[10] [b]Weight equivalents of KMnO₄ relative to MWCNT weight in the starting material. [c]Weight gain (%) upon isolation of the product relative to the starting weight of MWCNTs. [d]All scale bars are 100 nm; see Supporting Information for full-size high resolution images. [e]Weight percent remaining at 250 °C by TGA at 10 °C/min under Ar. [f]Weight percent remaining at 950 °C. [g]Recorded in water. [h]The darker portion in the TEM micrograph is part of the lacey carbon grid. [i]Preferred conditions for optimized GONRs.

Reaction 7 used a different acid reaction medium, trifluoroacetic acid (TFA) in the presence of trifluoroacetic anhydride (TFAA, to scavenge traces of water) with $5\times$ KMnO$_4$ at room temperature for 24 h. The resulting product was similar to that of reaction 6: stacked ribbons with minor unzipping of the MWCNTs and low levels of oxidation. There was no weight gain upon isolation of the product, the C:O ratio was high (7.6:1), and the TGA weight loss was low at only 6 wt %.

Reactions 8−11 used a series of conditions which varied the ratio of a second, weaker acid to H$_2$SO$_4$, as well as the reaction temperature; all reactions used $5\times$ KMnO$_4$. Reactions 8−10 used TFA as the second acid while reaction 11 substituted phosphoric acid (H$_3$PO$_4$) as the second acid. Reaction 8, carried out with a 1:1 ratio of H$_2$SO$_4$/TFA at room temperature for 24 h, produced stacked ribbons and partially unzipped MWCNTs with moderate levels of oxidation. The incomplete oxidation and exfoliation was supported by the small weight gain (34 wt %), C:O ratio of 4:1, TGA weight loss of 26 wt % at 950 °C, and UV λ_{max} of 265 nm.

Increasing the concentration of H$_2$SO$_4$ so that the H$_2$SO$_4$/second acid ratio is 9:1 results in nanoribbon formation and effective oxidation. This also confirms the necessity of ∼90% H$_2$SO$_4$ for complete exfoliation of GONRs. Reactions 9−11 all underwent ∼65 wt % gain upon isolation, had a C:O ratio of ∼1.5:1, and a TGA weight loss of ∼55 wt % at 950 °C. Reaction 9, however, was run at room temperature and TEM imaging and SEM imaging reveal that while ribbon formation occurred, the GONRs remained stacked and were not well exfoliated. When heat was applied to the reaction (65 °C for 2 h as is reactions 10 and 11), the GONRs were more exfoliated as identified by the presence of single ribbons by TEM and larger graphene-like networks observed with bulk SEM imaging (few tube structures were identified). Because reactions 10 and 11 produced exfoliated GONRs with similar properties, the identity of the second acid is not specific to TFA and may be extended to other more convenient and less expensive reagents such as H$_3$PO$_4$.

Reaction 12 used the same conditions as reaction 11 (9:1 H$_2$SO$_4$/H$_3$PO$_4$ 65 °C for 2 h) but increased the amount of KMnO$_4$ to $8\times$. This was performed to monitor the oxidation of the GONRs with increasing oxidizing agent. The product appeared to be more highly oxidized than that of reaction 11; while the isolated weight gain and C:O ratios were comparable, more weight was lost in the TGA (82% *versus* 58% at 950 °C) and the UV λ_{max} of the product of reaction 12 is blue-shifted further than any other sample studied (227 nm). Most striking, however, was the light brown color of the product of reaction 12; while all samples thus far classified as "highly oxidized" were a brown-black color, the color of the product of reaction 12 was a significantly lighter brown (similar to peanut butter) than the others. This confirms the results previously found[10] that the degree of oxidation can be controlled by the level of oxidizing agent, even above the limit which is needed to obtain highly oxidized and exfoliated GONRs.

Physical and Chemical Properties of GONRs Produced in the Presence of a Second Acid. The GONRs that were prepared in the presence of a second acid were studied in further detail to examine if the presence of the second acid produced any differences in surface functionality, quality, and conductivity in the samples which resulted in
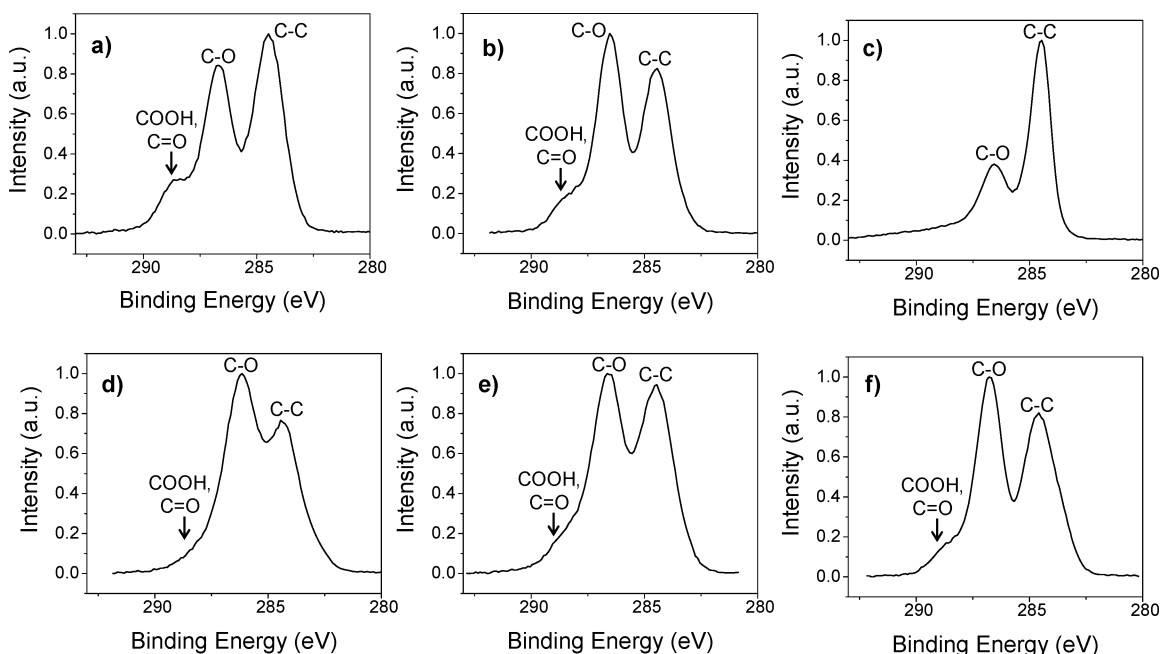

Figure 1. The XPS C1s spectra of the GONRs formed from reaction (a) 1, (b) 4, (c) 8, (d) 9, (e) 10, and (f) 11. The COOH shoulder at 289 eV is significantly less pronounced for GONRs in panels c−f than those in panels a and b and can be attributed to fewer COOH and C=O functionalities present in the GONRs prepared with a second weaker acid present.
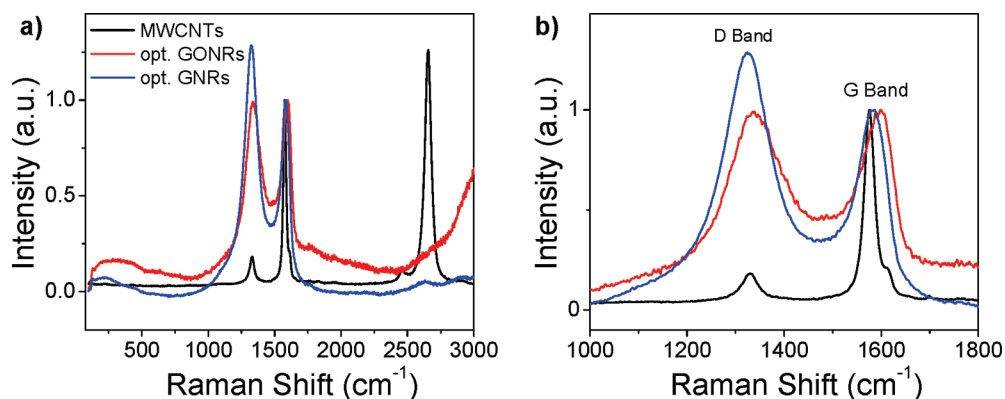
Figure 2. (a) The Raman spectra (633 nm excitation) of optimized GONRs before (red) and after (blue) reduction compared to the MWCNT starting material (black). The behavior is very similar to that observed for GONRs and GNRs previously reported.[10] After chemical reduction with hydrazine, the D:G peak ratio increases, as previously reported for chemically converted graphene.[15,16] **(b)** Expanded region of D and G bands from panel a. The peak intensities have been normalized to the G band.

oxidized nanoribbons. Reactions 10 and 11 revealed striking differences compared to those prepared by the original method with H_2SO_4 only (reactions 1−5). When 10% of a second acid (TFA or H_3PO_4) is added to the reaction mixture, XPS confirms that a significantly larger proportion of oxygen exists in the form of hydroxyl groups, and fewer oxygen is attributed to C═O and COOH functionalities. The XPS C1s spectra of six selected products from Table 1 are shown in Figure 1, and a clear difference in shape and peak identity is evident. The C1s spectra of GONRs from reactions 1 and 4 are shown in Figure 1a and 1b, respectively. Note that the XPS C1s spectrum of the GONRs produced from reaction 3 (not shown) is almost identical to that of 4. A distinct shoulder at 289 eV, assigned to carboxyl groups, is present in both products. The signals at

286−287 eV correspond to C−O, the intensity of which correlates to the level of oxidation within the sample while the signal at 284.9 corresponds to C−C bonds and is the most dominant peak in nonoxidized carbon species. The C1s spectra of the GONRs produced in the presence of a second acid from reactions 8, 9, 10, and 11 are given in Figure 1 panels c, d, e, and f, respectively. The low intensity of the C−O peak at 286 eV in Figure 1c (corresponding to reaction 8 prepared with 1:1 H_2SO_4/TFA) confirms that the ribbons are not as highly oxidized as those prepared with 90−100% H_2SO_4. Another important observation is the low intensity of the COOH shoulder at 289 eV for the GONRs prepared in the presence of the second acid; it is significantly less pronounced than in the C1s spectra of the GONRs (Figure 1a,b) produced with H_2SO_4 only. This correlates to fewer
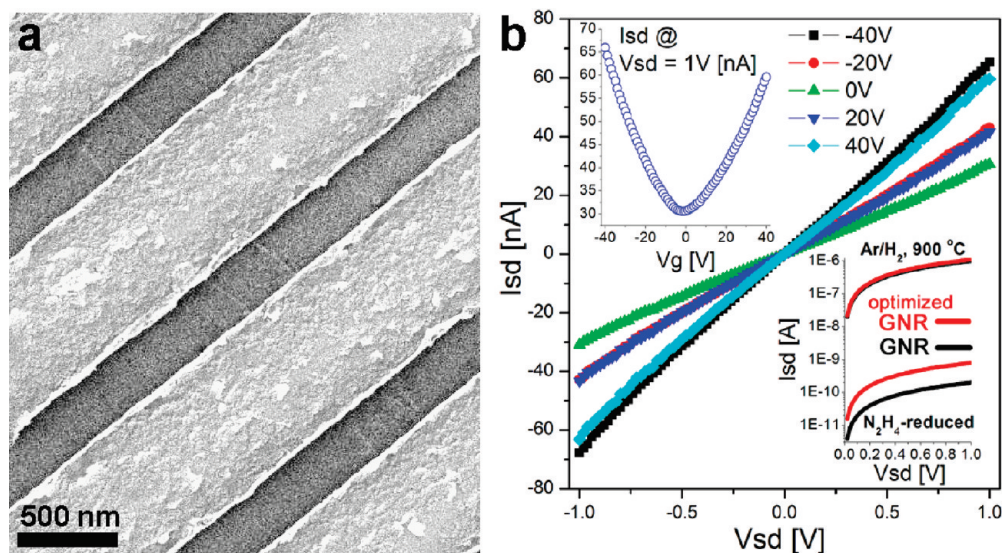
Figure 3. (a) SEM image of a typical four-terminal device based on a monolayer graphene nanoribbon (the GNR annealed in H_2/Ar at 900 °C for 1 h). The bright diagonal strips are Pt electrodes and the GNR is less visible, running from the top left of the image to the bottom right. **(b)** Electric field effects for the electronic device based on a monolayer GNR reduced by hydrazine and then annealed in H_2/Ar at 300 °C for 30 min. I_{sd}−V_{sd} characteristics are shown at V_g ranging from −40 to 40 V. Top inset shows transfer characteristics for the same device. Bottom inset shows logarithmic I_{sd}−V_{sd} characteristics for the monolayer optimized and unoptimized GNRs reduced either by hydrazine (two bottom curves) or by hydrazine and subsequent annealing in H_2/Ar at 900 °C for 1 h (two top curves). Each I−V curve is averaged for 4−10 similar devices.
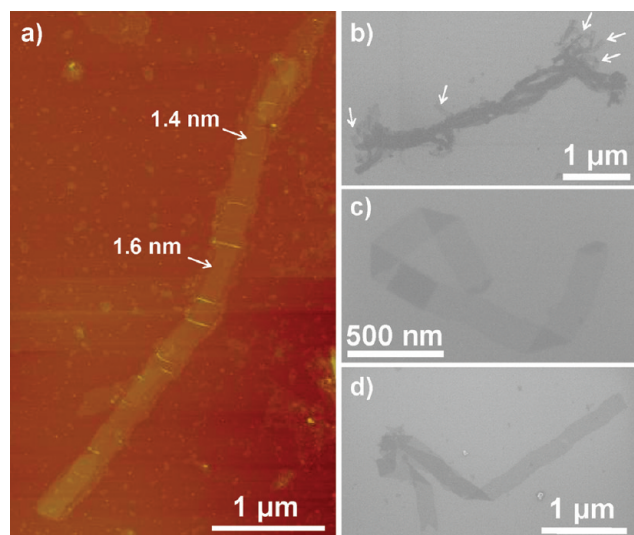
Figure 4. (a) AFM image of a bilayer optimized GONR that is ~5 μm long prepared under the conditions of reaction 11. The values of the heights at the locations indicated are 1.4 and 1.6 nm; the horizontal lines in the GONRs are buckles. (b−d) SEM images of GONRs (from reaction 11) on a SiO₂ surface. The width of the GONRs indicated in the agglomerate of panel b are all <100 nm. The images in panels c and d also show what are probably monolayer GONRs; this identification is based on studying the transparency to the electron beam of many samples.[17]

COOH and C═O functionalities present in the optimized GONRs prepared with the second acid present.

Raman spectroscopy (633 nm laser excitation) was used to further evaluate the structure of the optimized
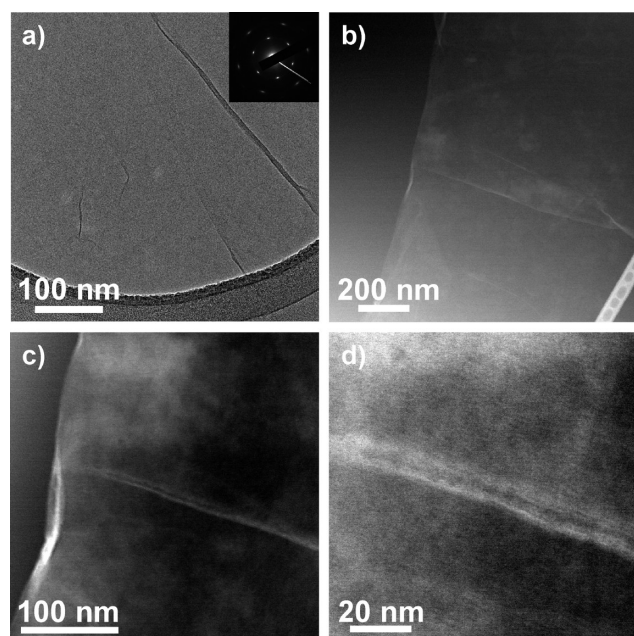
Figure 5. (a) Bright-field TEM image of an optimized GONR prepared from reaction 11 with the corresponding electron diffraction pattern (inset). The smooth ribbon surface and sharp, hexagonal diffraction pattern (inset) indicate the high-quality of the ribbons formed. The black curved structure at the bottom is part of the lacey carbon grid. (b−d) HAADF TEM images on one optimized GONR at increasing magnification from panels b to d. The uniformity of the atomic structure is apparent in that there are few instances of disruption in the contrast.

GONRs before and after chemical reduction by treatment with hydrazine to form graphene nanoribbons (GNRs). Hydrazine has previously been shown to be an effective agent for deoxygenation of GONRs and GO resulting in an increase in electrical conductivity.[10,13,15,16] Similar to what has been reported for GO and the unoptimized ribbons, the G band (1594 cm^{-1}) broadens after oxidation with appearance of the D band at 1363 cm^{-1} (Figure 2). Upon reduction, aromaticity is restored to the system and it is initially expected for the G peak to accordingly increase in intensity. However, in agreement with previous reports for chemically reduced GONRs and GO,[10,15] the D:G ratio increases after reduction. It is hypothesized that reduction increases the number of small domains of aromaticity responsible for the D peak, but not necessarily their overall size, which is responsible for the G peak.[15] In addition, the increased edge effects due to the narrow width of ribbons *versus* graphene could enhance this observation.

For the further comparison of optimized and unoptimized GNRs, the electrical properties were studied. Nanoribbons of both types were first hydrazine-reduced and then deposited onto Si/SiO₂ substrates as previously described.[17] Figure 3a shows an SEM image of a typical four-terminal electronic device based on a monolayer nanoribbon. All fabricated devices of both optimized and unoptimized GNRs exhibited an ambipolar electric field effect typical for graphene.[10,18] Interestingly, we found that the conductivities of hydrazine-reduced optimized GNRs were up to an order of magnitude higher than those of hydrazine-reduced unoptimized GNRs, though after annealing in Ar/H₂ at high temperatures this difference became far less significant. The electrical conductivity of monolayer GNRs on SiO₂ substrates was ~35 S/cm (averaged for 10 similar devices) after annealing in H₂/Ar at 900 °C for 1 h. For similar optimized GNRs we have measured ~40 S/cm (averaged for four similar devices). We note though that previous studies of the electronic properties of reduced GO flakes have revealed a large variability in the conductivity of presumably similar monolayer flakes.[19] Therefore, further studies to elucidate the electrical properties of optimized GNRs in more detail, including statistical analysis of the properties on a large number of unoptimized and optimized GNR devices, are in order and currently underway.

The overall morphology and physical structure of the optimized GONRs, specifically the product of reaction 11, was investigated using SEM and atomic force microscopy (AFM). It was found that compared to the unoptimized GONRs prepared without the second acid, the optimized GONRs are longer with higher edge linearity.[10] AFM imaging, such as the representative image shown in Figure 4a, revealed long ribbons (>5 μm) with straight edges and widths ranging from 75−200 nm. SEM imaging (Fig-

ure 4b−d) of optimized GONRs on a SiO$_2$ surface revealed mono- and few-layered ribbons several micrometers in length, with straight edges and uniform widths. Also significant is the width of the ribbons observed in the agglomerate in Figure 4b; the majority of ribbons identified have widths <100 nm, confirming that the addition of 10% of a second acid prevents oxidative consumption of the narrow-width ribbons. Monolayer GONRs, as shown in Figure 4c,d, as well as few-layered GONRs (Figure 4a) were present. The height of ~1.5 nm for a bilayer GONR is double the theoretically calculated height of 0.75 nm for a monolayer of GO, as the oxygen-containing functionalities on each side add additional height over that of the parent graphene.[20]

To study the quality and integrity of the nanoribbon surface, that is, to determine if there are holes present in the basal plane, high resolution TEM (HR-TEM) imaging and high angle annular dark-field (HAADF) TEM imaging were performed on both optimized and unoptimized GONRs. TEM images obtained with a HAADF detector are very sensitive to changes in specimen composition with the intensity varying monotonically with composition and specimen thickness.[21] Thus, HAADF imaging is highly sensitive to variations in the atomic structure of the sample and should effectively identify regions of defects and/or interruptions in the carbon plane. Figure 5a shows a bright-field HR-TEM image of a portion of an optimized GONR from reaction 11 with its corresponding electron diffraction pattern. The sample appears to be uniform and smooth over the entire region, and the hexagonal diffraction pattern corresponds to a crystalline graphite structure. Figure 5 panels b−d show three HAADF images, each taken of the same region of the GONR at increasing magnification. The atomic structure of the GONR appears uniform, with little disruption in the contrast indicating few defects. This is further confirmed by comparing HAADF and HRTEM images (Figure 6a−d) of GONRs prepared without a second acid (reaction 1) to optimized GONRs prepared with 10% H$_3$PO$_4$ (reaction 11); there is a clear difference in the structural uniformity. The HAADF of unoptimized GONRs (Figure 6a) shows changes in contrast throughout the entire imaged area; dark "spotty" patches corresponding to disruptions, including holes in the basal plane, can be identified. Comparison of the bright field TEM images in Figure 6c−e of unoptimized and optimized GONRs show similar observations. At comparable magnification, the optimized GONRs appear to have a smoother surface with fewer defects and/or holes than the unoptimized GONRs.

Proposed Reaction Mechanism. As previously reported,[10] the mechanism for the MWCNT opening is based upon literature precedent for the oxidation of alkenes by permanganate in acid. The proposed first step in the process is manganate ester formation (**2**
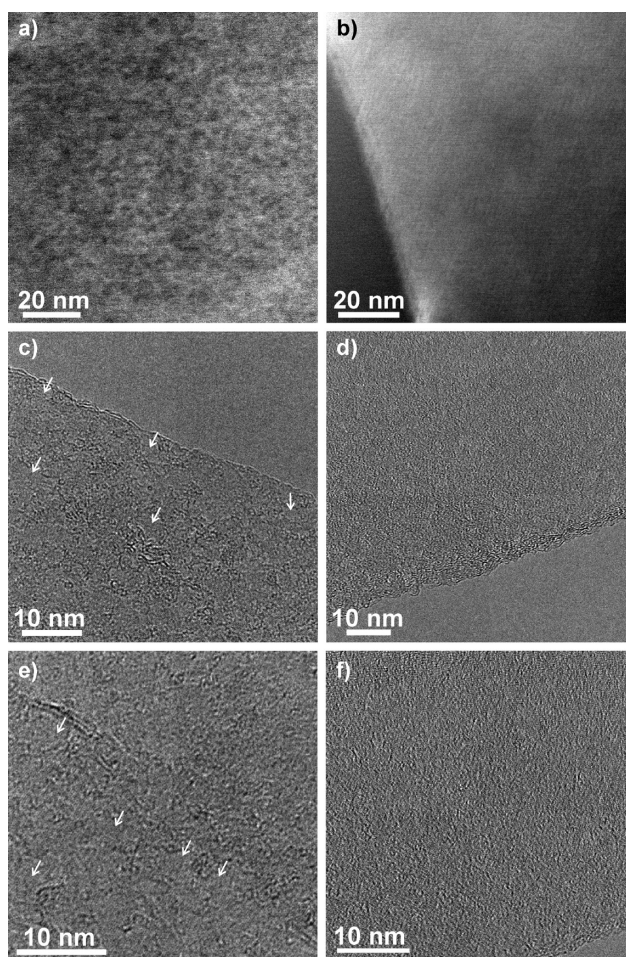

Figure 6. TEM images comparing the surface quality of unoptimized GONRs (a, c, e) and optimized GONRs (b, d, f). HAADF TEM images of (a) unoptimized GONR and (b) optimized GONR. The smooth surface of the optimized GONR is apparent by uniform contrast over the entire area; the unoptimized GONR has changing contrast with a spotty appearance indicative of nonuniformity in the atomic structure.[12] (c−f) Bright-field HRTEM images of unoptimized GONRs (c, e) and optimized GONRs (d, f). Close examination of the unoptimized GONR images reveals possible small holes and defects (a few indicated by white arrows) that make the surface appear roughened. The optimized GONR surface, on the other hand, is smoother in appearance with very few features that indicate defects.

in Scheme 1) as the rate-determining step, and further oxidation is possible to afford the dione (**3**) in the dehydrating medium.[22] Juxtaposition of the buttressing ketones distorts the β,γ-alkenes (red in **3**) making them more prone to the next attack by permanganate. As the process continues, the buttressing-induced strain on the β,γ-alkenes lessens since there is more space for carbonyl projection; however, the bond-angle strain induced by the enlarging hole (or tear if originating from the end of the nanotube) would make the β,γ-alkenes (**4** in Scheme 1) increasingly reactive. Hence, once an opening is initiated, its further opening is enhanced relative to an unopened tube or to an uninitiated site on the same tube. The ketones can be further converted, through their O-protonated forms, to the carboxylic acids[23] that will line the edges of the
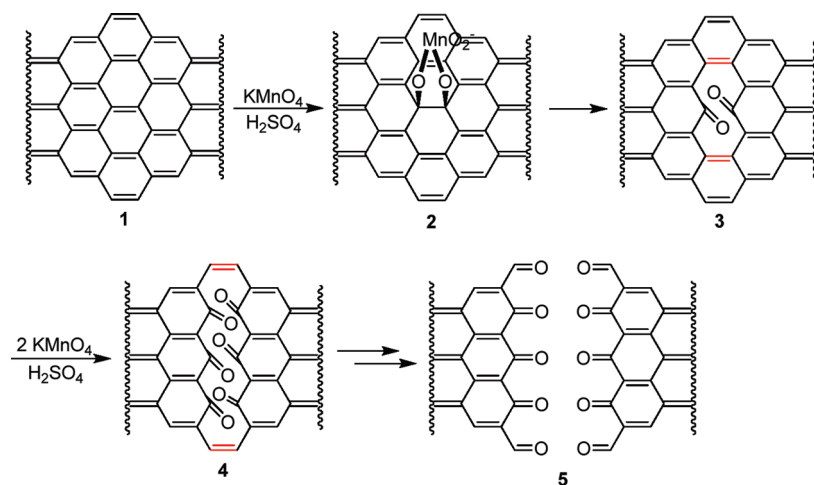
Scheme 1. The proposed chemical mechanism of nanotube unzipping. The manganate ester in 2 could also be protonated. The β,γ-alkenes (red in 3 and 4) are distorted owing to the buttressing ketones; the resulting bond-angle strain promotes further reaction at these sites.

nanoribbons. Finally, relief of the bond-angle strain when the nanotube opens to the graphene ribbon (**5** in Scheme 1) slows further dione formation and cutting.[22] *Ab-initio* DFT calculations have shown that this mechanism of unzipping results in zigzag ribbon edges.[24] It is also important to note that the presence of a second acid such as TFA or H$_3$PO$_4$ does not change the overall process through which unzipping of the MWCNT occurs. The kinetics of unzipping resemble that of chain-reaction polymerization: propagation must occur much faster than initiation, otherwise such straight and even edges would not be observed owing to numerous initiation sites on the MWCNT sidewall. Once the rate-limiting forma-
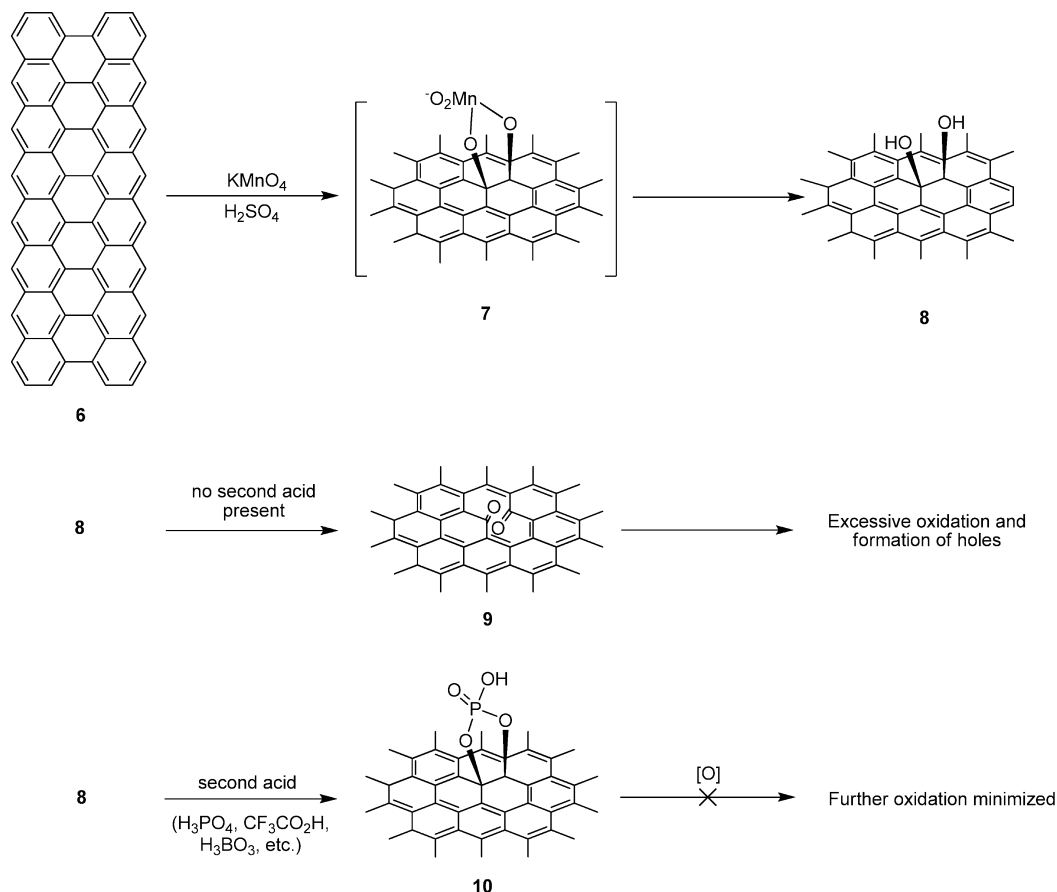
Scheme 2. Proposed mechanism for the effect of the second acid in preventing over-oxidation of the nanoribbons once they form from a MWCNT. The manganate ester in 7 could also be protonated. The key step is formation of the cyclic intermediate 10, resulting in protection of the vicinal diols (8) formed during the oxidation.

tion of the manganate ester species (**2**) occurs, the oxidative unzipping occurs on a faster time scale.

A proposed mechanism for the participation of the second acid in the oxidization of MWCNTs that results in GONRs is given in Scheme 2. It is thought that the second acid improves the chemoselectivity by minimizing the oxidation process. After initial manganate ester formation (**7** in Scheme 2), the vicinal diols that are formed will eventually cleave at the carbon—carbon bond between them, giving dione **9** and a new hole in the nanoribbon. Destructive oxidation throughout the structure then occurs and leads to defects and irreversible changes in the basal planes that cannot be repaired with chemical reduction. However, when an acid such as H_3PO_4 is present, it will protect the vicinal diols by forming cyclic structure **10**, thus preventing or retarding overoxidation to the diones. While the second acid will slow both the dione formation in the nanotube (**3**) and the nanoribbon (**9**), dione formation is essential for the unzipping and the source of ribbon defect formation. But the unzipping process must remain the faster of the two processes because of the curvature-induced strain in the tubular π-structure. This is reflected in the product mixture: consumption of the nanotubes and production of intact (uncut) ribbons. We have carried out this higher-selective process using not only TFA and H_3PO_4, but also polyphosphoric $(HO(PO_2OH)_xH)$, metaphosphoric $((HPO_3)_x)$, and boric acid (H_3BO_3). These latter three additives gave similar selectivity effects. Any reagent convertible to these acids under the reaction conditions such as corresponding salts, anhydrides, mixed anhydrides, and esters is expected to afford similar protection. The general requirements for the protective group are high rate of reaction with the diols, redox inactivity under the reaction conditions, and spontaneous hydrolysis upon subsequent aqueous workup.

CONCLUSIONS

Variations in the reaction conditions for the synthesis of GONRs[10] including the acid medium, time, and temperature were explored to determine the significance of each variable and to further elucidate the mechanism of interaction of the acid medium and oxidizing agent with the MWCNTs. It was found that sufficient H_2SO_4 (~90 vol %) was crucial for complete formation and exfoliation of the nanoribbons; in addition, elevation of the reaction temperature to 60 °C was necessary. Most interesting, however, was that addition of 10 vol % of a second acid such as TFA or H_3PO_4 greatly enhanced the quality of the nanoribbons that are produced. The new nanoribbons have a higher degree of oxidation (diols) but lower levels of hole formation that bear carbonyl and carboxyl moieties. The improved procedure did not result in the digestion of the thinner, <100 nm in width, nanoribbons. This also maximizes the aspect ratio of the products obtained. These observations were confirmed by AFM, SEM, and TEM analysis; electrical measurements of ribbon devices revealed that the conductivities of hydrazine-reduced optimized GNRs were 2—20 times higher than those of hydrazine-reduced unoptimized GNRs. Though we previously reported the formation of narrow nanoribbons from single-walled carbon nanotubes using a $H_2SO_4/KMnO_4$ method at 55 °C,[10] we had noted that the narrow nanoribbons were severely entangled. This entanglement persists with these improved conditions, and methods are being sought to overcome this difficulty so that electrical characterization can be done. Once these challenges are solved, the results will be reported separately.

METHODS

Preparation of Nanoribbons. MWCNTs were used as received from Mitsui & Co., Ltd. (Lot No. 05072001K28). These MWCNTs (MWNT-7) are now produced in the same manner but under the sole oversight of Hodogaya Chemical Co., Ltd. and they can be purchased from that entity (2-4-1, Shiba Koen, Minato-Ku, Tokyo 105-0011, Japan, +81-3-6430-3600). The remaining chemicals were purchased from Sigma-Aldrich and used as received, except for the concentrated sulfuric acid (Fisher Scientific) and oleum (Alfa Aesar). Deionized (DI) water (18 MΩ resistivity) obtained from a NanoPure system (Barnstead, Dubuque, IA) was used throughout this work. *Note*: Once nanoribbons are formed, they must be manipulated only with gentle stirring or short exposure bath sonication; use of high shear homogenization, probe sonication, or cup-horn sonication will result in shortened GNRs. All suspensions were prepared with gentle magnetic stirring, unless otherwise indicated. Bath sonication was performed with a Cole Parmer ultrasonic cleaner, model 08849-00 for the specified amount of time.

Nanoribbon Formation. Formation of nanoribbons from MWCNTs *via* procedure 1—5 was carried out as previously described,[10] with variations in the time and temperature as noted. **Caution**: *Do not exceed ~0.5 wt %/vol, weight KMnO4 to volume of*

H_2SO_4. *It is reported that at much higher concentrations, namely 7 wt %/vol KMnO4 in H_2SO_4, the mixture can explode upon heating.*[25] Briefly, MWCNTs (150 mg, 12.5 mequiv of carbon) were suspended in 30 mL of concentrated H_2SO_4 for a minimum of 1 h and up to 12 h. KMnO4 (750 mg, 4.75 mmol) was then added, and the mixture was allowed to stir for 1 h at room temperature. The reaction was then heated according to the reaction specifications in Table 1. Reaction 1 was identical to the procedure previously described (gradual increase to 70 °C over a period of 1 h) while reaction 2 was maintained at room temperature for 2 h. Reaction 3 was heated to 60 °C for 1 h, reaction 4 was heated to 85 °C for 1 h, and reaction 5 was heated to 100 °C for 1 h. Upon completion, the mixture was removed from the heat source and allowed to cool to room temperature, followed by workup as described below.

Reaction 6. A 150 mg portion of MWCNTs was suspended in 15 mL of concentrated H_2SO_4 for 15 min. The reaction mixture was placed in an ice bath, and 15 mL of oleum (H_2SO_4, 20% free SO_3) was slowly added. The mixture was stirred for 1 h, during which time the temperature was allowed to equilibrate to 25 °C by removing/applying an ice bath as appropriate. KMnO4 (750 mg) was then added, and the mixture was allowed to stir for 24 h at room temperature. The product was isolated as described below.

Reaction 7. A 150 mg portion of MWCNTs was suspended in 60 mL of TFA and 15 mL of TFAA by stirring the mixture for 15 min followed by bath sonication for 10 min. $KMnO_4$ (750 mg) was then added, and the mixture was bath sonicated for an additional 5 min. The solution was allowed to stir at room temperature for 24 h, with intermittent bath sonication (5 min) every few hours. Before the reaction was quenched, the consumption of $KMnO_4$ was monitored by taking 0.1 mL aliquots of the reaction mixture and diluting them with 1 mL of water. When no purple color was detected, the reaction was complete, and the workup procedures followed as described below.

Reaction 8. A 150 mg portion of MWCNTs was suspended in 37.5 mL of TFA and 37.5 mL of H_2SO_4 by stirring the mixture for 15 min followed by bath sonication for 10 min. $KMnO_4$ (750 mg) was then added, and the mixture was bath-sonicated for an additional 5 min. The solution was allowed to stir at room temperature for 24 h, with intermittent bath sonication (5 min) every few hours. Before the reaction was quenched, the consumption of $KMnO_4$ was monitored by taking 0.1 mL aliquots of the reaction mixture and diluting them with 1 mL water. When no purple color was detected, the reaction was complete and the workup procedures followed as described below.

Reactions 9 and 10. A 150 mg portion of MWCNTs was suspended in 36 mL of H_2SO_4 by stirring the mixture for a period of 1 h. TFA (4 mL) was then added, and the mixture was allowed to stir another 15 min before the addition of $KMnO_4$ (750 mg). For reaction 9, the reaction mixture was allowed to stir at room temperature for 24 h; for reaction 10, the reaction mixture stirred 1 h at room temperature and 2 h at 65 °C. Once the contents had cooled, the workup procedure was followed as described below.

Reaction 11. A 150 mg portion of MWCNTs was suspended in 36 mL of H_2SO_4 by stirring the mixture for a period of 1 h. H_3PO_4 (85%, 4 mL) was then added, and the mixture was allowed to stir another 15 min before the addition of $KMnO_4$ (750 mg). The reaction mixture was then heated at 65 °C for 2 h, and then allowed to cool to room temperature before product isolation as described below.

Reaction 12. A 150 mg portion of MWCNTs were suspended in 36 mL of H_2SO_4 by stirring the mixture for a period of 1 h. H_3PO_4 (85%, 4 mL) was then added, and the mixture was allowed to stir another 15 min before addition of $KMnO_4$ (1.2 g). The reaction mixture was heated at 65 °C for 2 h, then allowed to cool to room temperature before product isolation occurred as described below.

Workup Procedures. The products obtained from reactions 1−6 were worked up by pouring the cooled reaction mixture onto 400 mL of ice containing 5 mL of 30% H_2O_2 (to prevent precipitation of insoluble MnO_2). After vacuum filtration through a PTFE membrane (5.0 μm pore size), the solid was removed and stirred in 150 mL of water for 30 min, followed by bath sonication for 15 min. The material was coagulated by the addition of 20 vol % concentrated HCl (30 mL). The solid was filtered through a PTFE membrane (0.45 μm pore size) followed by removal of the solid, stirring in 150 mL of ethanol for 30 min, and bath sonication for 15 min. The material was coagulated by the addition of 100 vol % ether (150 mL) followed by filtration through a PTFE membrane (0.45 μm pore size). The final product was washed 2× with ether (50 mL each) and dried *in vacuo* to give the following yields: (1) 360; (2) 189; (3) 308; (4) 293; (5) 204; (6) 150 mg.

Reactions 7 and 8. The reaction mixture was poured onto ice (100 mL) containing H_2O_2 (30%, 5 mL) and filtered through a PTFE membrane (5.0 μm pore size) to give a black solid. The solid was washed with 20 vol % HCl (2 × 60 mL) and redispersed in ethanol (100%, 120 mL) with stirring (30 min) and bath sonication (15 min) before filtering through the same PTFE membrane. The product was washed 2× with ethanol (15 mL each), 2× with ether (15 mL each), and dried *in vacuo* to give the following yields: (7) 150; (8) 201 mg.

Reactions 9 and 10. The dispersion was poured onto 120 mL of ice containing H_2O_2 (30%, 5 mL), filtered through a PTFE membrane (5.0 μm pore size), and washed 3× with 10 vol % HCl (40 mL each). The solid was then dispersed in ethanol (100%, 30 mL) by stirring (30 min) and bath sonication (15 min). Ether (20 mL) was added to coagulate the product, which was again fil-

tered over the same PTFE membrane. The remaining solid was washed 2× with ether (50 mL each) and dried *in vacuo* to give the following yields: (9) 240; (10) 248 mg.

Reaction 11. The reaction mixture was poured onto 100 mL of ice containing H_2O_2 (30%, 5 mL). The product was allowed to coagulate (no stirring) for 14 h. The top portion was decanted from the solid, and the remaining portion was filtered over a 200 nm pore size PTFE membrane. The brown filter cake was washed 2× with 20% HCl (6 mL each), resuspended in H_2O (60 mL) by stirring for 2 h, and recoagulated with HCl (30%, 40 mL). The product was filtered on the same PTFE membrane and then dispersed in ethanol (100%, 40 mL) for 2 h with stirring. Ether (60 mL) was then added to the suspension, and the mixture was allowed to coagulate for 1 h before filtering through a 200 nm pore size PTFE membrane. The remaining solid was washed 2× with ether (10 mL each) and vacuum-dried to yield 267 mg of product.

Reaction 12. The reaction mixture was poured onto 100 mL of ice containing H_2O_2 (30%, 5 mL). The resulting light-brown colored precipitate was collected on a 200 nm pore size PTFE membrane, washed 2× with HCl (20 vol %, 6 mL each) and resuspended in H_2O (60 mL) by stirring for 2 h. Then HCl (30 vol %, 60 mL) was added to coagulate the product, which was then collected on the same PTFE membrane, washed 2× with HCl (20%, 6 mL each), and dispersed in ethanol (40 mL) for 2 h with stirring. Then the product was again coagulated by the addition of ether (60 mL), filtered over the same PTFE membrane, washed 3× with ether (6 mL each), and vacuum-dried to yield 215 mg of product.

Device Fabrication. Fabrication of graphene devices was performed by SEM (JEOL-6500) tracking of monolayer ribbons with the lengths >1 μm on the surface of 200-nm-thick dielectric SiO_2-covered, highly doped Si substrates followed by patterning 20-nm-thick Pt contacts *via* standard e-beam lithography and e-beam evaporation. Prior to testing, the devices used to produce the data in Figure 3b were annealed in H_2/Ar (1:1, <1 atm) atmosphere at 300−900 °C for 15−60 min. The electrical properties were tested using a probe station (Desert Cryogenics TT-probe 6 system) under vacuum with a chamber base pressure below 1×10^{-5} mm Hg. The devices were kept under vacuum for at least 1 d before the measurements. The $I-V$ data were collected using an Agilent 4155C semiconductor parameter analyzer.

Sample Analysis. TEM imaging was performed on a JEOL 2010. Samples were prepared by dispersing the nanoribbons in a 1:1 mixture of ethanol/water that was then dropped onto 300 mesh holey lacey carbon grids on a copper support (Ted Pella, Inc.). AFM images were obtained with a Nanoscope IIIa (Digital Instruments/Veeco Metrology, Inc.), operating in tapping mode, using 1−10 Ohm-cm phosphorus (*n*)-doped Si tips (Veeco, MPP-11100-140) at a scan rate of 2 Hz and 512 × 512 resolution. Samples for AFM analysis were prepared by spin coating aqueous solutions of nanoribbons at 3000 rpm onto a freshly cleaved mica surface (Ted Pella, Inc.) and the surface was rinsed during spinning with DI water and 2-isopropyl alcohol. UV−vis spectra were obtained on a Shimadzu UV-3101 PC with samples contained in 1-mL quartz cuvettes. FT-IR was acquired on a Nicolet FTIR infrared microscope with an attenuated total reflectance (ATR) attachment. XPS was performed on a PHI Quantera SXM scanning X-ray microprobe with a pass energy of 26.00 eV, 45° takeoff angle, and a 100 μm beam size. TGA (Q50, TA Instruments) was performed from room temperature to 950 at 10 °C/min under argon. Raman spectroscopy was performed on a Renishaw Raman scope using a 633 nm He−Ne laser.

Supporting Information Available: Large size, high resolution TEM and SEM images, full UV−vis absorption spectra, and XPS

survey scans with atomic concentrations of all reaction products listed in Table 1 and MWCNTs. This material is available free of charge *via* the Internet at http://pubs.acs.org.

REFERENCES AND NOTES

1. Geim, A. K.; Novoselov, K. S. The Rise of Graphene. *Nat. Mater.* **2007**, *6*, 183–191.
2. Morozov, S. V.; Novoselov, K. S.; Katsnelson, M. I.; Schedin, F.; Elias, D. C.; Jaszczak, J. A.; Geim, A. K. Giant Intrinsic Carrier Mobilities in Graphene and Its Bilayer. *Phys. Rev. Lett.* **2008**, *100*, 016602.
3. Stankovich, S.; Dikin, D. A.; Dommett, G. H. B.; Kohlhaas, K. M.; Zimney, E. J.; Stach, E. A.; Piner, R. D.; Nguyen, S. T.; Ruoff, R. S. Graphene-Based Composite Materials. *Nature* **2006**, *442*, 282–286.
4. Bunch, J. S.; Verbridge, S. S.; Alden, J. S.; van der Zande, A. M.; Parpia, J. M.; Craighead, H. G.; McEuen, P. L. Impermeable Atomic Membranes from Graphene Sheets. *Nano Lett.* **2008**, *8*, 2458–2462.
5. Areshkin, D. A.; Gunlycke, D.; White, C. T. Ballistic Transport in Graphene Nanostrips in the Presence of Disorder: Importance of Edge Effects. *Nano Lett.* **2007**, *7*, 204–210.
6. Han, M. Y.; Oezyilmaz, B.; Zhang, Y.; Kim, P. Energy Band-Gap Engineering of Graphene Nanoribbons. *Phys. Rev. Lett.* **2007**, *98*, 206805.
7. Li, X.; Wang, X.; Zhang, L.; Lee, S.; Dai, H. Chemically Derived, Ultrasmooth Graphene Nanoribbon Semiconductors. *Science* **2008**, *319*, 1229–1232.
8. Jiao, L.; Zhang, L.; Wang, X.; Diankov, G.; Dai, H. Narrow Graphene Nanoribbons from Carbon Nanotubes. *Nature* **2009**, *458*, 877–880.
9. Campos-Delgado, J.; Romo-Herrera, J. M.; Jia, X.; Cullen, D. A.; Muramatsu, H.; Kim, Y. A.; Hayashi, T.; Ren, Z.; Smith, D. J.; Okuno, Y.; *et al*. Bulk Production of a New Form of sp^2 Carbon: Crystalline Graphene Nanoribbons. *Nano Lett.* **2008**, *8*, 2773–2778.
10. Kosynkin, D. V.; Higginbotham, A. L.; Sinitskii, A.; Lomeda, J. R.; Dimiev, A.; Price, B. K.; Tour, J. M. Longitudinal Unzipping of Carbon Nanotubes to Form Graphene Nanoribbons. *Nature* **2009**, *458*, 872–876.
11. Lerf, A.; He, H.; Forster, M.; Klinowski, J. Structure of Graphite Oxide Revisited. *J. Phys. Chem. B* **1998**, *102*, 4477–4482.
12. Mkhoyan, K. A.; Contryman, A. W.; Silcox, J.; Stewart, D. A.; Eda, G.; Mattevi, C.; Miller, S.; Chhowalla, M. Atomic and Electronic Structure of Graphene-Oxide. *Nano Lett.* **2009**, *9*, 1058–1063.
13. Eda, G.; Fanchini, G.; Chhowalla, M. Large-Area Ultrathin Films of Reduced Graphene Oxide as a Transparent and Flexible Electronic Material. *Nat. Nanotechnol.* **2008**, *3*, 270–274.
14. Dzhabiev, T. S.; Denisov, N. N.; Moiseev, D. N.; Shilov, A. E. Formation of Ozone during the Reduction of Potassium Permanganate in Sulfuric Acid Solutions. *Russ. J. Phys. Chem.* **2005**, *79*, 1755–1760.
15. Stankovich, S.; Dikin, D. A.; Piner, R. D.; Kohlhaas, K. A.; Kleinhammes, A.; Jia, Y.; Wu, Y.; Nguyen, S. T.; Ruoff, R. S. Synthesis of Graphene-Based Nanosheets *via* Chemical Reduction of Exfoliated Graphite Oxide. *Carbon* **2007**, *45*, 1558–1565.
16. Tung, V. C.; Allen, M. J.; Yang, Y.; Kaner, R. B. High-Throughput Solution Processing of Large-Scale Graphene. *Nat. Nanotechnol.* **2009**, *4*, 25–29.
17. Sinitskii, A.; Fursina, A. A.; Kosynkin, D. V.; Higginbotham, A. L.; Natelson, D.; Tour, J. M. Electronic Transport in Monolayer Graphene Nanoribbons Produced by Chemical Unzipping of Carbon Nanotubes. *Appl. Phys. Lett.* **2009**, *95*, 253108.
18. Novoselov, K. S.; Geim, A. K.; Morozov, S. V.; Jiang, D.; Katsnelson, M. I.; Grigorieva, I. V.; Dubonos, S. V.; Firsov, A. A. Two-Dimensional Gas of Massless Dirac Fermions in Graphene. *Nature* **2005**, *438*, 197–200.
19. Gomez-Navarro, C.; Weitz, R. T.; Bittner, A. M.; Scolari, M.; Mews, A.; Burghard, M.; Kern, K. Electronic Transport Properties of Individual Chemically Reduced Graphene Oxide Sheets. *Nano Lett.* **2007**, *7*, 3499–3503.
20. Schniepp, H. C.; Li, J.-L.; McAllister, M. J.; Sai, H.; Herrera-Alonso, M.; Adamson, D. H.; Prud'homme, R. K.; Car, R.; Saville, D. A.; Aksay, I. A. Functionalized Single Graphene Sheets Derived from Splitting Graphite Oxide. *J. Phys. Chem. B* **2006**, *110*, 8535–8539.
21. Midgley, P. A.; Weyland, M. 3D Electron Microscopy in the Physical Sciences: The Development of Z-Contrast and EFTEM Tomography. *Ultramicroscopy* **2003**, *96*, 413–431.
22. Wolfe, S.; Ingold, C. F.; Lemieux, R. U. Oxidation of Olefins by Potassium Permanganate. Mechanism of α-Ketol Formation. *J. Am. Chem. Soc.* **1981**, *103*, 938–939.
23. Banoo, F.; Stewart, R. Permanganate Oxidation of Aromatic Alcohols in Acid Solution. *Can. J. Chem.* **1969**, *47*, 3199–3205.
24. Rangel, N. L.; Sotelo, J. C.; Seminario, J. M. Mechanism of Carbon Nanotubes Unzipping into Graphene Ribbons. *J. Chem. Phys.* **2009**, *131*, 031105.
25. Olley, R. H.; Bassett, D. C. An Improved Permanganic Etchant for Polyolefines. *Polymer* **1982**, *23*, 1707–1710.